

Transverse spin angular momentum of a space-time surface plasmon polariton wave packetNaoki Ichiji ^{1,2}, Daigo Oue ^{3,4,5}, Murat Yessenov,⁶ Kenneth L. Schepler ⁶, Ayman F. Abouraddy,⁶ and Atsushi Kubo ^{7,*}¹*Graduate School of Pure and Applied Sciences, University of Tsukuba, 1-1-1 Tennodai, Tsukuba-shi, Ibaraki 305-8571, Japan*²*Institute of Industrial Science, The University of Tokyo, 4-6-1 Komaba, Meguro-Ku, Tokyo 153-8505, Japan*³*Instituto de Telecomunicações, Instituto Superior Técnico, University of Lisbon, 1049-001 Lisbon, Portugal*⁴*Department of Physics, Kyoto University, Kyoto 606-8502, Japan*⁵*The Blackett Laboratory, Imperial College London, London SW7 2AZ, United Kingdom*⁶*CREOL, The College of Optics & Photonics, University of Central Florida, Orlando, Florida 32816, USA*⁷*Faculty of Pure and Applied Sciences, University of Tsukuba, 1-1-1 Tennodai, Tsukuba-shi, Ibaraki 305-8571, Japan*

(Received 15 February 2023; revised 10 June 2023; accepted 13 June 2023; published 28 June 2023)

In addition to longitudinal spin angular momentum (SAM) along the axis of propagation of light, spatially structured electromagnetic fields such as evanescent waves and focused beams have recently been found to possess transverse SAM in the direction perpendicular to the axis of propagation. In particular, the SAM of surface plasmon polaritons (SPPs) with spatial structure has been extensively studied in the last decade after it became clear that evanescent fields with spatially structured energy flow generate three-dimensional spin texture. Here we present numerical calculations of the space-time surface plasmon polariton (ST-SPP) wave packet, a plasmonic bullet that propagates at an arbitrary group velocity while maintaining its spatial distribution. ST-SPP wave packets with complex spatial structure and energy flow density distribution determined by the group velocity are found to propagate with accompanying three-dimensional spin texture and finite topological charge density. Furthermore, the spatial distribution of the spin texture and topological charge density determined by the spatial structure of the SPP is controllable, and the deformation associated with propagation is negligible. ST-SPP wave packets, which can stably transport customizable three-dimensional spin textures and topological charge densities, can be excellent subjects of observation in studies of spin photonics and optical topological materials.

DOI: [10.1103/PhysRevA.107.063517](https://doi.org/10.1103/PhysRevA.107.063517)**I. INTRODUCTION**

Spin angular momentum (SAM) associated with the rotation of electromagnetic polarization [1–3] plays an important role in both classical and quantum optics [4–11]. While the SAMs of light have been studied for nearly a century, most discussions until the 2000s focused on the longitudinal SAM (l -SAM), which is the component parallel to the propagation axis. However, Aiello *et al.* and Bliokh *et al.* reported that optical SAM also has a component perpendicular to the propagation axis, transverse SAM (t -SAM) [12–14]. t -SAM has recently received much attention as it is responsible for a longstanding problem of polarization-dependent beam shift (the Imbert-Fedorov shift) [12,13,15], has been given new rotational degrees of freedom in optical manipulation [16–18], and provides strong light-matter coupling, which cannot be achieved by ordinary polarizations [19]. t -SAM is proportional to the rotation of the energy flow density of the electromagnetic field and arises when the Poynting vector of the electromagnetic field has a spatial gradient in the plane normal to the propagation direction of the optical field, such as in tightly focused beams [20,21], guided light [22], interference beats between two plane waves [23], and evanescent

fields [24]. Studies related to t -SAM have been conducted from a wide range of perspectives, including control of SAM with hyperbolic metasurfaces [25], and spin and momentum densities in water waves [26].

Surface plasmon polaritons (SPPs), which are surface electromagnetic waves confined at the metal-insulator interface, are accompanied by an evanescent field that decays in the perpendicular direction to the interface and thus exhibits t -SAM in the in-plane direction (t -SAM_∥) [27–31]. The direction of the t -SAM_∥ of the SPP is fixed according to the energy propagation direction, resulting in a broken time-reversal symmetry. Hence, as a counterpart of a quantum spin Hall effect of light [32,33], the t -SAM_∥ of SPPs has garnered widespread interest in the field of spin photonics [34–38].

Furthermore, when the SPP has a two-dimensional spatial structure at the confined interface, its t -SAM is not limited to the in-plane component, but also includes an out-of-plane component (t -SAM_⊥) [39–47]. The existence of both t -SAM_⊥ and t -SAM_∥ components of SPP indicates that the SPP can have a three-dimensional arrangement of spin textures and thus a finite surface area on the Poincaré polarization vector sphere [48–51]. Efforts to generate topologically stable three-dimensional spin vector fields by preparing a vortexlike energy flow have been actively pursued in the context of topological quasiparticles [39,40]. The introduction of integer topological charges into SPPs using the designed

*kubo.atsushi.ka@u.tsukuba.ac.jp

light-SPP coupler or vortex beam has enabled the demonstration of various plasmonic topological quasiparticles, including plasmonic spin skyrmion [39,42,44,52], topological melon structure [40,53], and topological plasmonic field [54,55] and spin [41,43] lattice structures. However, the spin textures of SPPs discussed in previous studies are typically excited at specific coordinates and do not involve spatial movement, such as propagation. While numerous studies have examined and experimentally realized the motion control of magnetic skyrmions [56–60], only a few have considered the spatial movement of the spin texture of SPPs [61,62].

Shi *et al.* recently formulated the t -SAM of the structured electromagnetic guided waves and experimentally demonstrated the t -SAM $_{\perp}$ of SPP waves with inhomogeneous energy flow density, such as Cosine SPP and Airy SPP waves [46]. Their formulation of the SAM suggests that all SPP waves with both spatial structure and energy flow should be accompanied by t -SAM $_{\perp}$, even if these SPP fields are topologically uncharged. Therefore, temporal variation of the SPP fields with spatial structure, such as SPP wave packets with short temporal widths [63], steering SPP beams excited by achromatic incident waves [64], and plasmonic bullets with confinement in all dimensions [65], are expected to be accompanied by t -SAM $_{\perp}$ in their propagation. However, although several observations of t -SAM $_{\perp}$ associated with SPPs have been reported [47], the migration of t -SAM $_{\perp}$ caused by propagating SPP fields has rarely been investigated.

Here, we present theoretical calculations of the t -SAM $_{\perp}$ for the space-time SPP (ST-SPP) wave packet, a newly proposed type of SPP wave packet classified as a plasmonic bullet [66]. ST-SPP wave packets are structured SPPs with artificially designed propagation characteristics achieved through precise adjustments to the spatial and temporal frequencies of each frequency component of the SPP wave packet. The concept of designing propagation characteristics by adjusting the time-space-frequency correlation of a wave packet was initially proposed and experimentally demonstrated for light pulses and referred to as space-time (ST) waves [67–69]. ST-SPP wave packets have been theoretically shown to possess attractive properties such as diffraction-free and dispersion-free propagation invariance and arbitrary group velocities. Efforts to experimentally excite and observe them are ongoing [70,71].

In this study, we conducted an examination of the three-dimensional spin arrangement of ST-SPP wave packets through calculations of each electromagnetic component and energy flow density. Our calculations revealed that ST-SPP wave packets possess a three-dimensional spin texture and a finite topological charge density. The spin texture and topological charge density of ST-SPPs with propagation invariance were found to be spatially robust and maintain a stable spatial distribution during propagation. Interestingly, the topological charge density of ST-SPP wave packets exhibited spatial distributions with only opposite signs on the left and right, with positive and negative positional relationships reversing depending on the group velocity. The proposed calculation results open up the possibility of constructing plasmonic topological quasiparticles and manipulating excited structured SPP waves, which may have potential applications in optical information transfer and optical trapping.

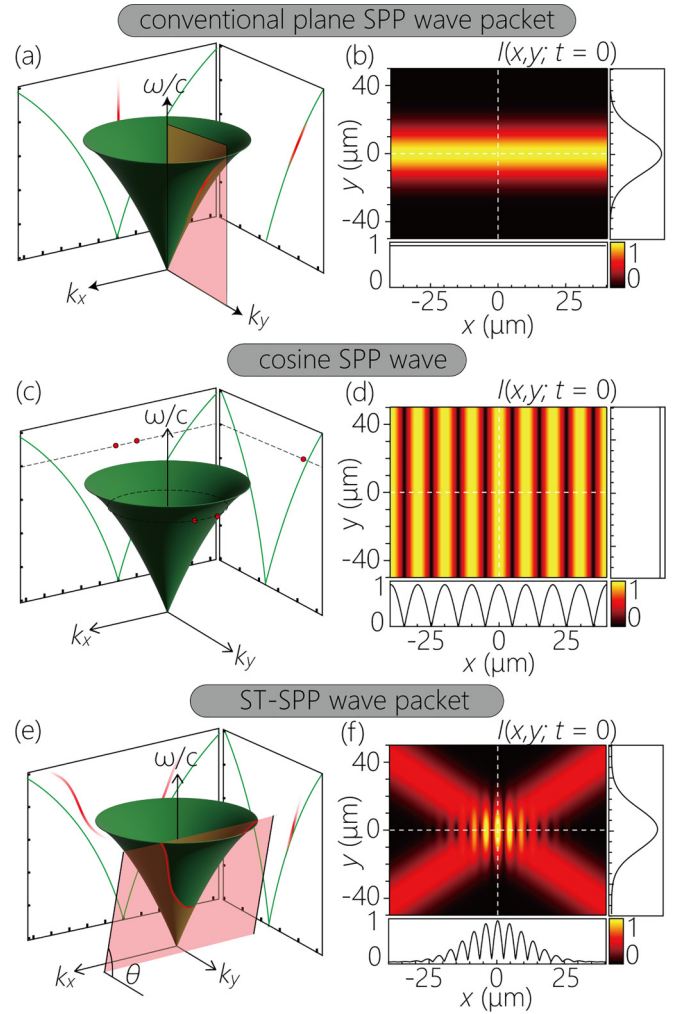


FIG. 1. (a) The spectral representation of a conventional plane SPP wave on the surface of the SPP-light cone $k_x^2 + k_y^2 = k_{sp}^2$. (b) Spatial distribution of the field intensity of a conventional plane SPP wave in physical space, $I(x, y; t = 0)$. (c), (d) Same as (a), (b), but for a Cosine SPP wave. (e), (f) Same as (a), (b), but for an ST-SPP wave. The black lines in the side and bottom panels in (b), (d), and (f) are cross sections through the field distributions in the main panels at $x = 0$ and $y = 0$. Each profile in (b), (d), and (f) is normalized by each maximum value.

II. ST-SPP WAVE PACKET

To describe the dispersion relation of a wave packet with a two-dimensional spatial distribution, such as an ST-SPP wave packet, a three-dimensional spatiotemporal spectral diagram consisting of one frequency axis and two wave-number axes is useful. While the light cone of the light in a vacuum is a cone $k_l = \omega/c$, the three-dimensional spatiotemporal correlation of SPP, the SPP light cone, has a curved surface that reflects the dispersion of SPP (Fig. 1) [66,72],

$$k_{sp} = \frac{\omega}{c} \sqrt{\frac{\epsilon_m(\omega)\epsilon_d}{\epsilon_m(\omega) + \epsilon_d}}, \quad (1)$$

where $\epsilon_{d(m)}$ is the relative permittivity of the dielectric (metal).

In the case of the conventional pulsed SPP wave with uniform intensity in the transverse direction, the spectral support domain of the SPP wave packet corresponds to the intersection of the SPP-light cone and $k_x = 0$ plane [Fig. 1(a)]. We choose the y direction as the axial propagation direction and define the z direction as the surface normal of the interface between metal and dielectric so that the SPP is localized on the xy plane. The out-of-plane component of the electric field distribution of the conventional SPP plane wave packet with finite width along the propagation direction [Fig. 1(b)] is given by $\int d\omega \tilde{E}(\omega)e^{i(k_y y - \omega t)}$, where ω is the temporal angular frequency and $\tilde{E}(\omega)$ is the pulse spectrum, the Fourier transform of $E(t)$ at $y = 0$. The free-space pulse used to excite the SPP has the form

$$E(t) = E_0 e^{-i\omega_0 t} \exp\left(-\frac{t^2}{[\Delta T/(2 \ln 2)]^2}\right), \quad (2)$$

where $\Delta T = 100$ fs, $\omega_0/(2\pi) = 375$ THz (800 nm wavelength), and E_0 is the amplitude of the electric field. The dielectric is assumed to be vacuum ($\epsilon_d = 1$) and the metal is gold (Au). We employ the Lorentz-Drude model [73] for $\epsilon_m(\omega)$. Experimentally, the conventional plane SPP wave packet corresponds to a wave packet excited by a linear light-SPP coupling structure with sufficiently long length, such as a slit or gratings [74,75]. The propagation of a conventional SPP wave on the dispersive sample surface is inevitably accompanied by deformation and chirping due to the frequency dependence of the group velocity [63].

As a comparison, the spectral support domain of the Cosine SPP wave [76] is shown in Fig. 1(c). The Cosine SPP waves are a spatial pattern generated by the interference of two SPPs, corresponding to the two-wave interference in free space [23]. On the SPP-light cone surface, the spectral support domain of the Cosine SPP wave is defined by two points that have identical k_y components and two k_x components equal in magnitude but with opposite signs. The spatial field distribution E_z^{cos} is given by

$$\begin{aligned} E_z^{\text{cos}}(\mathbf{x} | \omega) &= \frac{1}{2} \tilde{E}(\omega) (e^{i(k_x x + k_y y - \omega t)} + e^{i(-k_x x + k_y y - \omega t)}) \quad (3) \\ &= \tilde{E}(\omega) \cos(k_x x) e^{+i(k_y y - \omega t)}, \quad (4) \end{aligned}$$

where we have defined $\mathbf{x} = (x, y, t)$. In this study, E_z is calculated for the insulator side ($z > 0$). Note that k_x and k_y are the real components of the wave vector along the transverse (x) and axial (y) coordinates, respectively, which satisfy the relation $k_x^2 + k_y^2 = k_{\text{sp}}^2$. The interference between the two plane waves generates a periodic cosine-shaped field distribution in the transverse direction, as its intensity profile is shown in Fig. 1(d).

Importantly, the axial wave number of the Cosine SPP wave, $k_y = \sqrt{k_{\text{sp}}^2 - k_x^2}$, can be arbitrarily set in the range $0 < k_y < k_{\text{sp}}$ by properly selecting k_x . Therefore, by making all frequency components of the SPP wave packet into Cosine SPP waves with designed k_y , structured SPP wave packets with arbitrary dispersion on the propagation axis can be constructed. The concept of designing the dispersion relation on the propagation axis by strictly adjusting k_x and k_y has already been experimentally demonstrated for light pulses in free space and is known as a space-time (ST) wave packet

[67–69]. ST wave packets with a variety of novel propagation characteristics have been reported, including a diffraction-free property [67], arbitrary group velocity [77], acceleration and deceleration in unprecedented ranges [78,79], the introduction of dispersion properties into a light pulse in free space [80,81], and nondispersive propagation in a dispersive media [82].

The spectral support domain of an ST-SPP wave packet, which is the target of this study, is defined as a one-dimensional trajectory at the intersection of the SPP-light cone, given by Eq. (1), with a spectral plane $\Omega = (k_y - k'_o)c \tan \theta$, that is parallel to the k_x axis and makes an angle θ with the k_y axis [Fig. 1(e)], where k'_o is the SPP wave number evaluated at the carrier frequency [i.e., $k'_o = k_{\text{sp}}(\omega = \omega_o)$] and $\Omega = \omega - \omega_o$ is the frequency measured with respect to ω_o .

The projection of the spectral support domain onto the $(k_y, \frac{\omega}{c})$ plane is a straight line, and thus the group velocity $\tilde{v}_g = d\omega/dk_y = c \tan \theta$ is a constant independent of ω . Each component of the spatial field distribution of the ST-SPP wave packet on the $z = 0^+$ plane, E_x^{ST} , E_y^{ST} , and E_z^{ST} , is given by [46] (see, also, the Appendix A for details)

$$E_x^{\text{ST}}(\mathbf{x}) = i \int d\omega \frac{k_z}{k_{\text{sp}}^2} \frac{\partial}{\partial x} E_z^{\text{cos}}(\mathbf{x} | \omega), \quad (5)$$

$$E_y^{\text{ST}}(\mathbf{x}) = i \int d\omega \frac{k_z}{k_{\text{sp}}^2} \frac{\partial}{\partial y} E_z^{\text{cos}}(\mathbf{x} | \omega), \quad (6)$$

$$E_z^{\text{ST}}(\mathbf{x}) = \int d\omega E_z^{\text{cos}}(\mathbf{x} | \omega), \quad (7)$$

where $k_z = \sqrt{k_1^2 \epsilon_m - k_{\text{sp}}^2}$ is the wave number in the surface normal that determines the exponential decay in the z direction [$\mathbf{E}(x, y, z; t) = \mathbf{E}(\mathbf{x})e^{ik_z z}$]. Remember that k_z and k_{sp} are functions of ω .

While the k_x of the conventional SPP wave packet is always 0, that of the ST-SPP wave packet varies with frequency to keep $d\omega/dk_y = c \tan \theta$. As a result, ST-SPP wave packets possess a finite transverse bandwidth Δk_x and thus exhibit spatial confinement in both the axial and transverse directions. Previous experiments on ST wave packets in free space and simulation results of the ST-SPP wave packets have shown that the spatial distributions of the ST wave packets are X shaped. [see Fig. 1(f)] [69,71,83]. The ST-SPP wave packet with a characteristic X-shaped spatial distribution propagates toward the y direction with the designed group velocity $\tilde{v}_g = c \tan \theta$, maintaining the identical spatial distribution unless ohmic losses are considered [66].

Note that the calculations of ST-SPP wave packets in this paper are performed under the condition that (i) SPP attenuation is neglected and (ii) the wave source is of infinite width. With these assumptions, the ST-SPP wave packet constitutes a nondiffractive beam with an infinite propagation distance, a so-called infinite energy beam, and thus is experimentally unfeasible [84–86]. Nevertheless, this modeling is still valid enough to investigate a realistic ST-SPP for the following reasons: First, even if the SPP damping is taken into account, the spatial stability of the wave-packet shape and the distribution of the normalized t -SAM remain almost unchanged. Therefore, the attenuation does not affect the main conclusions about the spin texture and the topological charge density that we will discuss later. Second, properties of a realistic

finite-energy ST-SPP coincide with the case of the infinite-energy one when the SPP attenuation is taken into account.

A useful insight is obtained from the relation between the effective beam radius D and the propagation distance L_b in which the nondiffractive property of a finite-energy beam is maintained. In the case of the Cosine-Gauss plasmon beam, L_b is expressed as $L_b \sim D/\sin\alpha$, where α is the incident angle [76,87]. A finite-energy ST-SPP is generated by an incidence of an experimentally realizable ST wave with a regulated beam width D on a light-SPP coupler [70]. Therefore, the practical ST-SPP wave packet should possess a similar limitation.

In addition, the propagation distance of the ST wave is tied to the uncertainty in the spectral support domain [68,88]. The ideal ST wave, in which each spatial frequency (k_x) is associated with one temporal frequency (Ω) with unambiguous precision, is practically unfeasible because it requires infinite beam area. Realistically, experimental limitations in the generation of a ST wave such as a finite beam area and a related spectral resolving power of an optical system induce a fuzziness in the association between k_x and Ω (i.e., spectral uncertainty $\delta\Omega$). The $\delta\Omega$ regulates the limit of the propagation distance over which the ST wave maintains propagation invariance, L_{ST} [69,88]. This restriction is also valid for the ST-SPP wave packet [66]. The L_{ST} is usually two orders of magnitude larger than the Rayleigh length [69].

However, in practice, the SPP attenuation length κ , rather than L_b or L_{ST} , regulates the propagation distance of ST-SPP because κ limits the effective wave source width. The main contribution to the formation of the ST-SPP wave packet comes from wave sources located within a distance $\sim\kappa$ from the center of the wave-packet emission. This means that if the excitation beam is sufficiently wider than κ , the difference from the case of infinite source width becomes almost negligible. Since κ is typically a few tens of micrometers (e.g., $\kappa \approx 45 \mu\text{m}$ for SPP on a Au surface with the excitation light wavelength of 800 nm), this condition is practical.

III. ENERGY FLOW DENSITY

For an SPP wave with an evanescent field, the SAM can be calculated as follows:

$$\mathbf{S} = \frac{1}{4\omega} \text{Im}(\epsilon \mathbf{E}^* \times \mathbf{E} + \mu \mathbf{H}^* \times \mathbf{H}). \quad (8)$$

The electric field \mathbf{E} is given by Eqs. (5)–(7), and the magnetic field \mathbf{H} is calculated from E_z by employing the Maxwell equations [46] (see Appendix A). The asterisks signify their complex conjugates. We can confirm the SAM is a divergenceless vector field, $\nabla \cdot \mathbf{S} = 0$. This implies that the SAM is the rotation of another vector field. Indeed, taking the rotation of the canonical decomposition of momentum density, $\nabla \times \epsilon\mu(\mathbf{P} - \mathbf{P}_o) = \nabla \times \nabla \times \mathbf{S}/2$, where $\mathbf{P} = \text{Re}(\mathbf{E}^* \times \mathbf{H})/2$ is the total energy flow density, and $\mathbf{P}_o = \text{Im}[\mu^{-1}\mathbf{E}^* \cdot (\nabla)\mathbf{E} + \epsilon^{-1}\mathbf{H}^* \cdot (\nabla)\mathbf{H}]/(4\omega)$ is the orbital contribution, we can find the following relationship [46,89–92]:

$$\mathbf{S} = \frac{2}{\omega^2} \nabla \times (\mathbf{P} - \mathbf{P}_o) = \frac{1}{2\omega^2} \nabla \times \mathbf{P}. \quad (9)$$

From Eq. (9), it can be confirmed that the SAM of the SPP is represented by a rotation of the energy flow density. In Fig. 2, we plot the in-plane components of the energy flow density in the ST-SPP wave packets calculated at different group velocities. In this study, the group velocity of the conventional SPP wave packet at the center frequency, $v_{sp}[\omega/(2\pi) = 375 \text{ THz}] = 0.91c$, is defined as the boundary velocity for superluminal ($\tilde{v}_g > v_{sp}$) and subluminal ($\tilde{v}_g < v_{sp}$) (c : Speed of light in vacuum). The tilt angle of the spectral plane θ is determined by the designed group velocity, $\theta = \tan^{-1}(\tilde{v}_g/c)$. In this paper, we set $\omega_o/(2\pi) = 360 \text{ THz}$ (390 THz) for the superluminal (subluminal) ST-SPP wave packet. The spectral projections onto the (k_y, ω) and (k_x, ω) planes for an ST-SPP with $\tilde{v}_g = c$, i.e., the superluminal ST-SPP wave packet, are plotted in Fig. 2(c).

The energy flow density in the axial direction P_y indicates the direction in which the ST-SPP wave packet propagates. The spatial distribution of P_y shown in Fig. 2(a) corresponds to the spatial distribution of the field intensity profile shown in Fig. 1(f). In contrast to P_y , which is positively valued everywhere, the spatial distribution of P_x (i.e., the energy flow density in the direction transverse to the propagation axis) is composed of two diagonal branches with opposite signs [see Fig. 2(b)]. These two branches are constructed by the $+k_x$ and $-k_x$ components of the ST-SPP, indicated by red and blue lines in Fig. 2(c), respectively. As a result of the destructive interference between the two branches, P_x vanishes on the x and y axes (at $t = 0$). Figures 2(d)–2(f) show the Poynting vector and the spectral projections for the subluminal ST-SPP wave packet, $\tilde{v}_g = 0.8c$. In the subluminal and superluminal ST-SPP wave packets, the energy flow in the propagation direction P_y exhibits a similar spatial distribution. In contrast, the energy flow in the transverse direction P_x is reversed [Fig. 2(e)]. In Fig. 2(g), the calculation for one branch consisting only of the $+k_x$ components [red lines in Figs. 2(c) and 2(f)] is presented, which is useful to understand the spatial distribution of the ST-SPP wave packet and the energy flow. The typical spatial distributions of P_y and P_x of the $+k_x$ branches are plotted in the left panels. While P_x and P_y are positive regardless of the group velocity, the spatial distribution of the branches show a marked dependence on the group velocity. In the superluminal regime, the angle between the branches and the propagation axis is positive, $\alpha > 0$, while in the subluminal regime, $\alpha < 0$. This implies the counterintuitive fact that the spatial angle of the branch is determined independently of the direction of the energy flow (see Appendix B). In addition, the intensity distributions also show that P_y and P_x have different dependencies on the group velocity. P_y and P_x at $(x, y) = (0, 0)$ for various group velocities ranging from $0.7c$ to $1.1c$ are plotted in the right panel. P_y reaches the maximum value when $\tilde{v}_g = v_{sp}$ and decreases as the \tilde{v}_g deviates from v_{sp} , and vice versa for P_x . Since the ratio of k_x and k_y represents the tilt angle of each frequency component, an increase in k_x tends to result in an increase in P_x in exchange for a decrease in P_y . It is also noteworthy that the variation of P_y is less than 1%, while that of P_x exceeds 50% in this calculation range. This correlation between P_y and P_x suggests that the controllable group velocity of the ST-SPP wave packet can be interpreted as the projection of the velocity of the diagonal branch onto the propagation axis, which is propagating in a slightly oblique

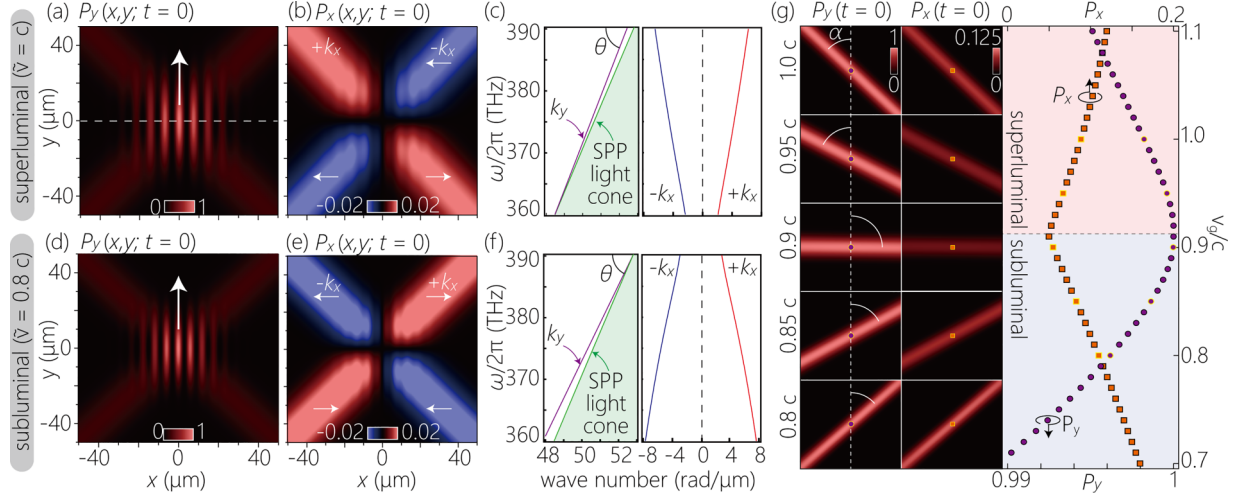


FIG. 2. The spatial distributions of the energy flow density for ST-SPP waves at $t = 0$. (a) P_y and (b) P_x components of the superluminal ST-SPP wave packet with $\tilde{v}_g = 1.0c$. (c) The spectral projections onto the (k_y, ω) and (k_x, ω) planes. (d)–(f) Same as (a)–(c), but for the subluminal ST-SPP wave packets with $\tilde{v}_g = 0.8c$. (g) Spatial distributions of the energy flow density of one of the branches comprising the ST-SPP wave packet calculated from the $+k_x$ components only. Each display region is entirely identical to (b) and (e). The intensities obtained at the $x = y = 0$ are plotted in the right panel as a function of group velocity. The maximum value of P_y at $\tilde{v}_g = v_{sp}$ was normalized to 1.

direction from the propagation axis. Note that the velocity projected on the propagation axis corresponds to the velocity of movement of the intersection point of the two branches for the ST-SPP wave packet consisting of $\pm k_x$ components.

IV. SPIN ANGULAR MOMENTUM

Figures 3(a)–3(c) show each component of the SAM of the superluminal ST-SPP wave packet, calculated from Eq. (8) at $\tilde{v}_g = c$. As the main component of t -SAM $_{\parallel}$ (S_x and S_y) arises

from the exponential decay of the in-plane energy flow density along the surface normal, we have $S_x \approx -[1/(2\omega^2)]\partial P_y/\partial z$ and $S_y \approx [1/(2\omega^2)]\partial P_x/\partial z$ and can confirm these are consistent with the spatial distribution of P_y and P_x [see Figs. 3(a) and 3(b)].

On the other hand, the t -SAM $_{\perp}$ (S_z) arises from the rotation of the in-plane energy flow of the SPP. As the y component of the energy flow is approximately 10 times larger than the x component, $P_y \gg P_x$, in this study [Fig. 2(g)], it dominantly contributes to the t -SAM $_{\perp}$, $S_z \approx [1/(2\omega^2)]\partial P_y/\partial x$.

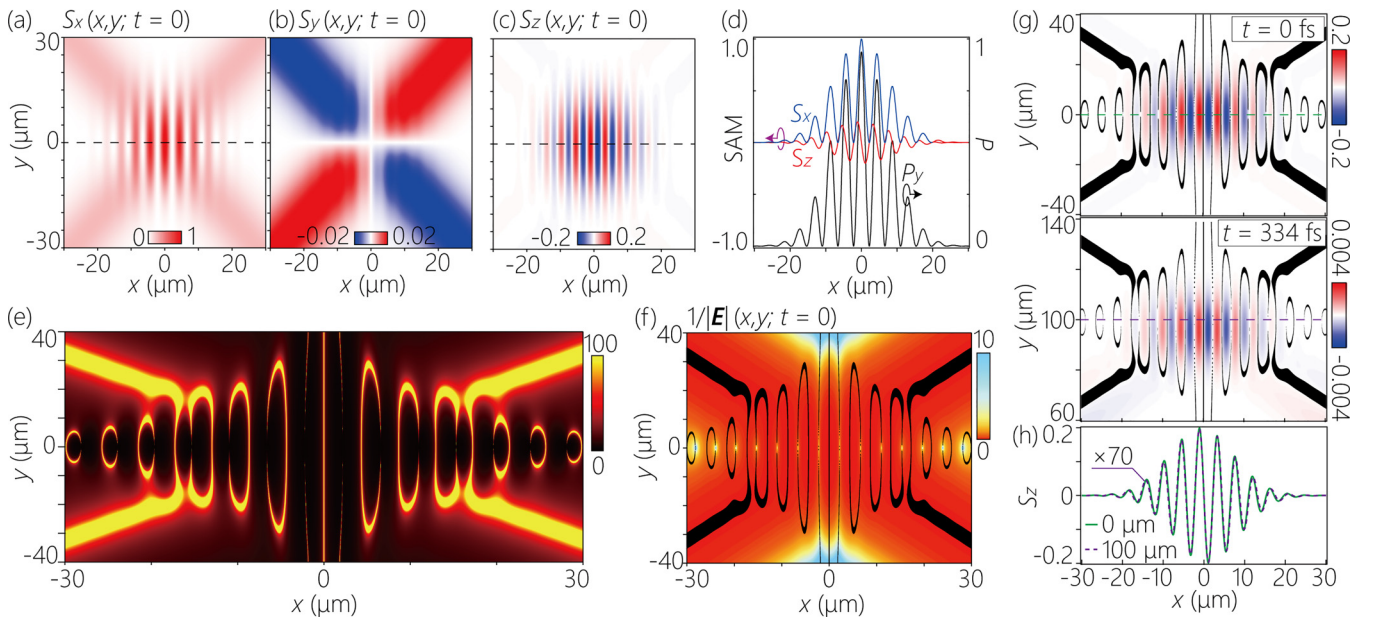


FIG. 3. (a)–(c) Spatial field distribution of the spin texture, (a) S_x , (b) S_y , and (c) S_z component. (d) Cross sections along the dashed lines in (a) and (c), and energy flow density in the propagation direction, P_y , obtained at corresponding positions. (e) The L-line singularity map of the in-plane polarization of SPP fields. (f) The inverse of the magnitude of the electric field distribution. The black lines represent the L-line calculated by taking the contour lines of (d) with a value of 100. (g) Spatial distributions of the t -SAM $_{\perp}$ and L-lines before and after propagation calculated at $t = 0$ and $t = 334$ fs. (h) The cross sections along the lateral direction at $x = 0$ μm and 100 μm .

Figure 3(d) shows the cross sections of the x and z components of the SAM along the x axis ($y = 0$) [dashed lines in Figs. 3(a) and 3(c)]. Note that the y component of the energy flow [dashed line in Figs. 2(a)] is also plotted in the same figure. The spatial distribution of the phase-matched S_x and $\pi/2$ -shifted S_z with respect to the P_y component is consistent with the SAM of the Cosine SPP wave reported previously [46].

To characterize the three-dimensional spin texture of the SAM, we evaluate where the ellipticity of the local polarization is minimal in the xy plane. This region corresponds to the equator of the Poincaré sphere and can be interpreted as the L-line region where the field is linearly polarized [93,94]. In Fig. 3(e), we plotted the L-line singularity map $|S|/S_z$. Note that the L-lines shown in Fig. 3(e) are not a one-dimensional trajectory, but have a finite width because the L-line map saturates in the region where S_z is smaller than 1%.

Because the t -SAM $_{\perp}$ of the ST-SPP wave packet is generated from the cosinelike spatial structure resulting from the interference between the $+k_x$ and $-k_x$ branches, there are almost no S_z components in regions where the two branches do not spatially overlap. Therefore, the X-shaped region without fringes of the ST-SPP wave packet exhibits linear polarization, which is the polarization state of the conventional SPP wave packet. In contrast, multiple split ring-shaped L-lines, which are derived from the spatial structure of the ST-SPP wave packet, are aligned along the x axis ($y = 0$) with their split points oriented in the opposite direction around the y axis. The split ring structures define perimeters where the t -SAM $_{\perp}$ of the ST-SPP wave packet is distributed on the plane, and the split points on the x axis are singularities where the electric field amplitude is zero. Around these discontinuous points, there is a steep gradient in the electric field intensity. In Fig. 3(f), we plot the L-line obtained from Fig. 3(e) overlaid on the inverse of the electric field distribution, $1/|E|$.

Although the calculations up to this point only considered the case $t = 0$ and propagation loss was not taken into account, the actual propagation of an ST-SPP wave packet on the dispersive metal surface has a frequency-dependent attenuation determined by the imaginary part of the dielectric function. The attenuation of the overall intensity is inevitable, and there will be a slight deformation where the ST-SPP wave packet has an ultrabroadband spectral width [66,70]. To estimate the spin texture stability of the ST-SPP wave packet, calculations of the ST-SPP wave packet before and after propagation were performed with an attenuation model that introduced propagation loss into Eqs. (5)–(7). The propagation loss at each frequency was calculated from $\text{Im}[\epsilon_m(\omega)]$. For each frequency component with a finite transverse wave number, which propagates in a slightly oblique direction, we define the distance of propagation $y/\cos(\phi)$, where ϕ is the angle between the propagation direction and the y axis, $\phi = \tan^{-1}(k_x/k_y)$. In Fig. 3(g), we plot the spatial distributions of the t -SAM $_{\perp}$ calculated by the attenuation model at $t = 0$ and $t = 334$ fs. The L-lines calculated at each time were also overlaid on the plots.

While the S_z distribution after propagation over ~ 100 μm shows an overall attenuation in intensity, the spatial distribution surrounded by the L-line is almost unchanged from

that before propagation. Moreover, the cross sections along the dashed lines in Fig. 3(g) almost overlap [see Fig. 3(h)]. This indicates that the deformation of the spin texture with propagation is marginal. Note that the shape of the S_z distribution in Fig. 3(g) is slightly skewed towards smaller values of y compared to the peak position of a lossless wave packet ($y = 100$ μm). This happens because the front part of the wave packet has a longer propagation distance than the tail part and therefore attenuates more strongly (see Appendix D). From these calculations, we conclude that the ST-SPP wave packet can transport the spin texture in a spatially stable manner of the order of the propagation length of the SPP.

V. TOPOLOGICAL CHARGE DENSITY

We next discuss the topological properties of ST-SPP based on the SAM textures obtained above. We calculate the topological charge density as in studies of topological spin quasiparticles, where the integration of the topological charge density over an area within the boundary of the quasiparticle provides the topological charge (skyrmion number) [39–45,49,53]. The topological charge density is defined by

$$D = \frac{1}{4\pi} \mathbf{S}' \cdot \left(\frac{\partial \mathbf{S}'}{\partial x} \times \frac{\partial \mathbf{S}'}{\partial y} \right), \quad (10)$$

where we have normalized the SAM, $\mathbf{S}' = \mathbf{S}/|S|$.

Figure 4(a) shows the calculated D map for an ST-SPP wave packet with $\tilde{v}_g = c$. The positions of the discretized spatial distribution of D correspond to the split points of the L-lines. One of the major characteristics of the D map is its reversed signs on the left and right sides: The spatial distribution exhibits perfect line symmetry around the x axis, with positive values for positive x and negative values for negative x . In addition, the D map for $\tilde{v} = 0.8c$ plotted in Fig. 4(b) shows a similar symmetric spatial distribution as in the case of $\tilde{v} = c$, but with opposite signs on the left and right. The left-right reversal and the group velocity-dependent reversal of the sign of D are explained by the spatial distribution of S_y . In Figs. 4(c) and 4(d), we plot each component of \mathbf{S}' (S'_x , S'_y , and S'_z) for the superluminal and subluminal ST-SPP waves shown in Figs. 4(a) and 4(b), respectively. As shown in Fig. 3, the t -SAM $_{\parallel}$ arising from the decay of evanescent fields has spatial distributions consistent with the in-plane component of \mathbf{P} , P_x and P_y . While S'_x is positive throughout the calculation region regardless of the group velocity, S'_y has a different sign in each quadrant. The sign is switched depending on whether the group velocity is subluminal or superluminal. On the other hand, the spatial distribution of t -SAM $_{\perp}$ is mainly determined by the partial differentiation of P_y in the x direction; it, therefore, does not exhibit quadrant dependence of the sign, unlike S'_y .

To examine the differences in the spatial distribution of each component in detail, the enlarged view around the split points is plotted in the top panels, one on the left (region L) and one on the right (region R). In contrast to the consistent spatial distribution of S'_x and S'_z , only the S'_y component shows the switched signs for right and left, and for superluminal and subluminal. From Eq. (10), we can confirm that the sign of D is switched when the two vector components of \mathbf{S}' are fixed, and only the sign on one component is switched.

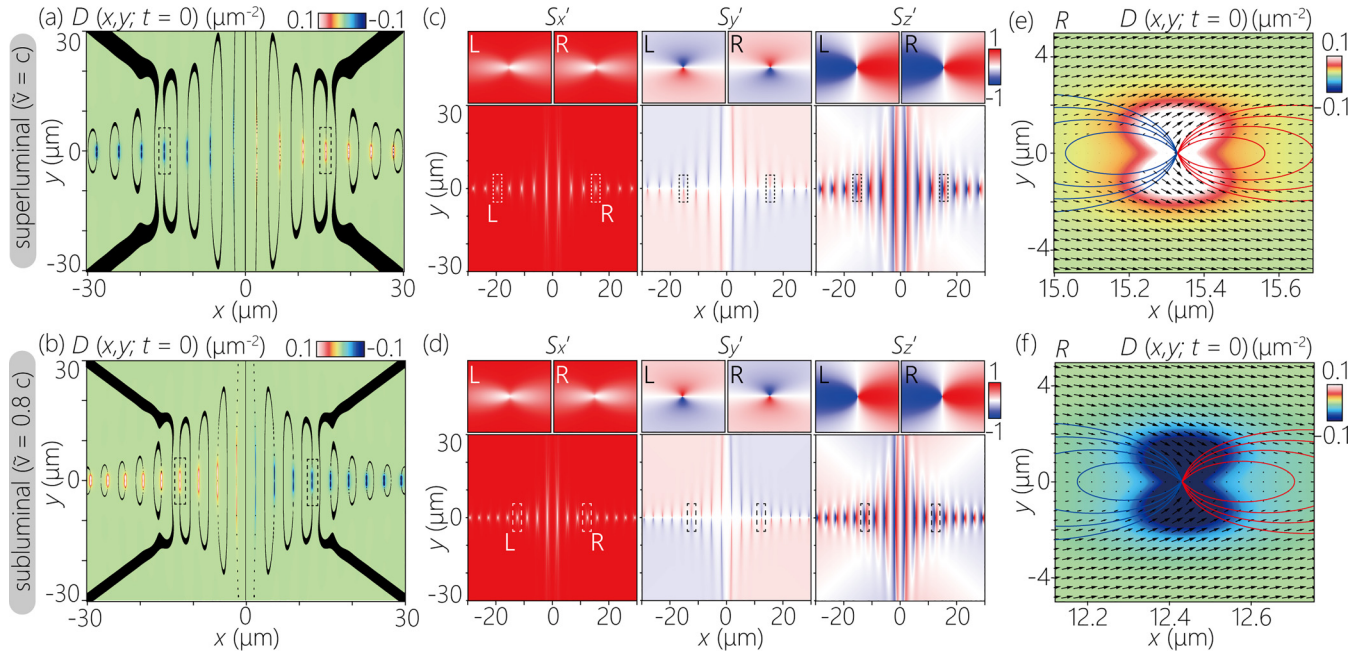


FIG. 4. (a), (b) Spatial distributions of the topological charge density D at $t = 0$ for (a) $\tilde{v} = c$, (b) $\tilde{v} = 0.8c$. The black lines represent the L-line calculated by $|S_x|/S_z$. The regions around the fourth split point on the left and right from the center are defined as L and R , respectively. (c), (d) Spatial distributions of each normalized SAM component, S'_x , S'_y , and S'_z , for (c) $\tilde{v} = c$ and (d) $\tilde{v} = 0.8c$. The expanded views of the dashed squares are plotted in the top panels. (e), (f) The expanded view of the right dashed square in (c) and (d) of the spatial distribution of each component of the normalized SAM. The vector plots show the in-plane components, and the color lines show the contour of the out-of-plane components (red: -0.9 to -0.6 , blue: 0.6 to 0.9). The color map represents the distribution of D .

This is consistent with the calculation results shown in Figs. 4(a)–4(d). It can also be seen that the in-plane and out-of-plane components of S' have complementary spatial distributions at the vicinity of the split points. Both S'_x and S'_y are zero at $y = 0$ and have a spatial distribution that extends toward the y direction from the split point of the L-line. In contrast, S'_z shows the maximum value at $y = 0$ and has a distribution that extends toward the x direction. The vector plots of the in-plane components of S' and the contour plots of the out-of-plane component superimposed on the D map plotted in Figs. 4(e) and 4(f) show more clearly the positional relationship of each S' component. The plotted areas correspond to the region R . The field distribution of the S_x in Figs. 4(c) and 4(d) and the direction of the in-plane components of the SAM in Figs. 4(e) and 4(f) indicate that S_x is dominant in most of the calculation region. Only in a limited region around the split points of the L-line does each component of SAM have comparable magnitudes, and D a finite value.

There have been a few methods used for experimental evaluations of D in topological SPP fields. One is to determine the t -SAM distribution from local Stokes parameters measured over the structured field. This method uses dielectric nanospheres as a probe to scatter the evanescent field of the SPP [39,95]. The other is to reconstruct the vector components of the electromagnetic field from the microscopic image of the field intensity by using Maxwell's equations. Phase-sensitive near-field scanning optical microscopy (NSOM) [54] and interferometric pump-probe photoemission electron microscopy (PEEM) [40,43,55] have been reported. Identifications of the electric fields, SAMs, L-lines, and topological charge densities of topological plasmonic skyrmions and skyrmion lattices

have been performed [44]. Similar techniques could also be applied to the ST-SPPs.

VI. DISCUSSION AND CONCLUSION

The propagation invariance of an ST-SPP preserves the wave-packet shape and the L-line structure, which forms the stable frame of the SAM texture. As discussed above, the propagation of the ST-SPP is accompanied by the propagation of topological charge densities with different signs on its left and right sides. In the case of a plasmonic spin skyrmion or meron, a phase singularity (C-point) exists in the core of the vortex where an in-plane rotating electric field (local circular polarization) is formed [39,40,42,44,49]. It corresponds to the north or the south pole of the Poincaré sphere; the local polarization is circularly polarized and the SAM vector points in the surface-normal direction. The field exhibits a 2π -phase rotation around the center with the angular momentum provided by the excitation light field or the geometrical charge of a coupling structure. The ST-SPP, in contrast, does not have the plasmonic vortex like the plasmonic spin skyrmion; the ST-SPP has an X-shaped electric field distribution, with each branch consisting of the $+k_x$ and $-k_x$ branch components of the spectral support domain [Figs. 1(f), 2(a)–2(f)]. In the central part of the X shape, the electric field forms a textured structure and oscillates at the central frequency of the wave packet (see Appendix B). In the areas on either side, “holes” in the electric field strength are lined up due to the interference between the $+k_x$ and $-k_x$ branches [Fig. 3(f)]. These holes are not accompanied by a 2π -phase rotation of the field and are therefore distinct from the central core of the plasmon

skyrmions mentioned above. Because the ST-SPP propagates at the group velocity v_{sp} , the energy flow density is inherently dominated by the positive-valued P_y component. The lack of negative P_y precludes generations of vortices around phase singularities. However, the periodic modulation of P_y intensity in the transverse direction is responsible for the surface-normal SAM [Fig. 3(d)]. The overall SAM vector distribution of ST-SPP is concentrated in the positive S_x , while it changes steeply only in the vicinity of the holes of the field. The SAM vector is not distributed over the hemisphere or the entire Poincaré sphere; therefore, the topological charge is neither half integer nor integer. However, the different branches consisting of the $+k_x$ and $-k_x$ components surrounding the hole generate S_y components of different signs, resulting in the winding of SAM and the related nonzero topological charge density D [Figs. 4(e) and 4(f)]. This nonzero D is specific to ultrashort ST-SPP wave packets, not to single-frequency SPP fields, because it originates from the spatial proximity of the $+k_x$ and $-k_x$ branches and thus should be associated with the geometry of the spectral support domain that generates the ST-SPP.

Since the SPP also has an evanescent field associated with electric polarization on the metal side, it would be useful to describe the SAM interaction with metal electrons and the relation to topological magnetic quasiparticles. First, the SAM in the metal comprises the circular motion of electrons or localized circular currents. As a result, magnetization due to the inverse Faraday effect is expected to occur within the metal [30,96–99]. The magnetic field can interact with the electron spin. Indeed, conduction electron spin currents can be driven by the SPPs at a single surface [100–102], a metallic film [103,104], and in graphene [105,106]. Second, the SAM vector in the Poincaré sphere is regarded as an optical correspondence of the magnetization vector in magnetic skyrmion systems. The topological charge density is a physical quantity that reflects the degree of twist in the local spin (magnetization) vector. In the context of magnetic topological spin textures, D can be related to as an emergent magnetic field b_{em} [56,107,108]. In two-dimension systems, the magnitude of the field vector directing the surface normal is proportional to D . Importantly, b_{em} is not merely a fictitious field, but can also interact with the spins of other electrons in solid materials. The interaction of b_{em} with electron spins via the magnetic moments described by the Landau-Lifshitz-Gilbert (LLG) equation has been experimentally confirmed [59,107,109–111]. This interaction, known as the topological Hall effect [112–114], has realized the manipulation of magnetic skyrmions by external currents. It is noteworthy that the *propagating topological charge density* was found in the context of SPPs, which belong to the class of optical topological systems. Furthermore, the correspondence between the magnetic topological systems and optical spin topological systems demonstrated in various previous studies suggests that the topological charge density calculated in this study can be considered as an optical emergent magnetic field that can interact with the spins of electrons in materials [115,116]. In addition, the propagation invariance and arbitrary group velocities of the ST-SPP wave packet enable adaptive transport of topological charge density with a stable spatial distribution across subluminal and superluminal regimes. Through the

experimental excitation of ST-SPP wave packets using a spatial light modulator (SLM), the intensity, spatial distribution, and polarity of D can be adjusted externally at the driving frequency of the SLM. This feature enables the exploration of novel opportunities to realize spin information transmission.

In conclusion, we have conducted numerical simulations to examine the spin texture in an ST-SPP wave packet, which is a type of plasmonic bullet that possesses propagation invariance at arbitrary group velocities. Our calculations reveal three-dimensional spin textures in these wave packets, which are found to have stable spatial distributions during propagation over distances of the order of the SPP propagation length. Furthermore, we have discovered that the ST-SPP wave packet also possesses a finite topological charge density, which exhibits a symmetric spatial distribution where only the sign differs between the left and right sides of the propagation axis. As the spin texture and topological charge density are determined by the gradient of the energy flow density, it is possible to design them by manipulating the ST-SPP wave packet. These findings suggest that three-dimensional localized electromagnetic fields can propagate with accompanying spin textures and may offer the possibility to observe optical topological particle propagation phenomena experimentally.

ACKNOWLEDGMENTS

A.K. thanks Y. Dai for the valuable discussions. This work was supported by the JSPS KAKENHI (Grants No. JP16823280, No. JP18967972, No. JP20J21825, No. JP23H04575), MEXT Q-LEAP ATTO (Grant No. JPMXS0118068681), and by the U.S. Office of Naval Research (ONR) under Contracts No. N00014-17-1-2458 and No. N00014-20-1-2789. D.O. is supported by the President's Ph.D. Scholarships at Imperial College London, by JSPS Overseas Research Fellowship, by the Institution of Engineering and Technology (IET), and by Fundação para a Ciência e a Tecnologia and Instituto de Telecomunicações under Project No. UIDB/50008/2020.

APPENDIX A: THE ELECTRIC AND MAGNETIC FIELD

The electric field brought about by an SPP is given by utilizing the transverse polarization basis with the SPP dispersion relation. As the SPP wave is a transverse magnetic mode, the electric field will be given, in terms of the Hertz potential [117–119], in the reciprocal space as

$$\mathbf{E} = \mathbf{k} \times \mathbf{k} \times \psi \mathbf{u}_z = (k_z \mathbf{k}_{\parallel} - |\mathbf{k}_{\parallel}|^2 \mathbf{u}_z) \psi, \quad (\text{A1})$$

where $\psi \mathbf{u}_z$ corresponds to the Hertz vector potential, and we defined the parallel component of the wave vector, $\mathbf{k}_{\parallel} = k_x \mathbf{u}_x + k_y \mathbf{u}_y$. The ratio of $E_{x,y}$ to E_z can be written as

$$\frac{E_{x,y}}{E_z} = \frac{k_z k_{x,y}}{-|\mathbf{k}_{\parallel}|^2} = \frac{ik_z \partial_{x,y}}{k_{sp}^2}. \quad (\text{A2})$$

Note that we have used the dispersion relation $|\mathbf{k}_{\parallel}|^2 = k_{sp}^2$ and replaced $k_{x,y} \rightarrow -i\partial_{x,y}$. Multiplying E_z from the right-hand side, we can get

$$\mathbf{E}_{\parallel} = \frac{ik_z}{k_{sp}^2} \nabla_{\parallel} E_z, \quad (\text{A3})$$

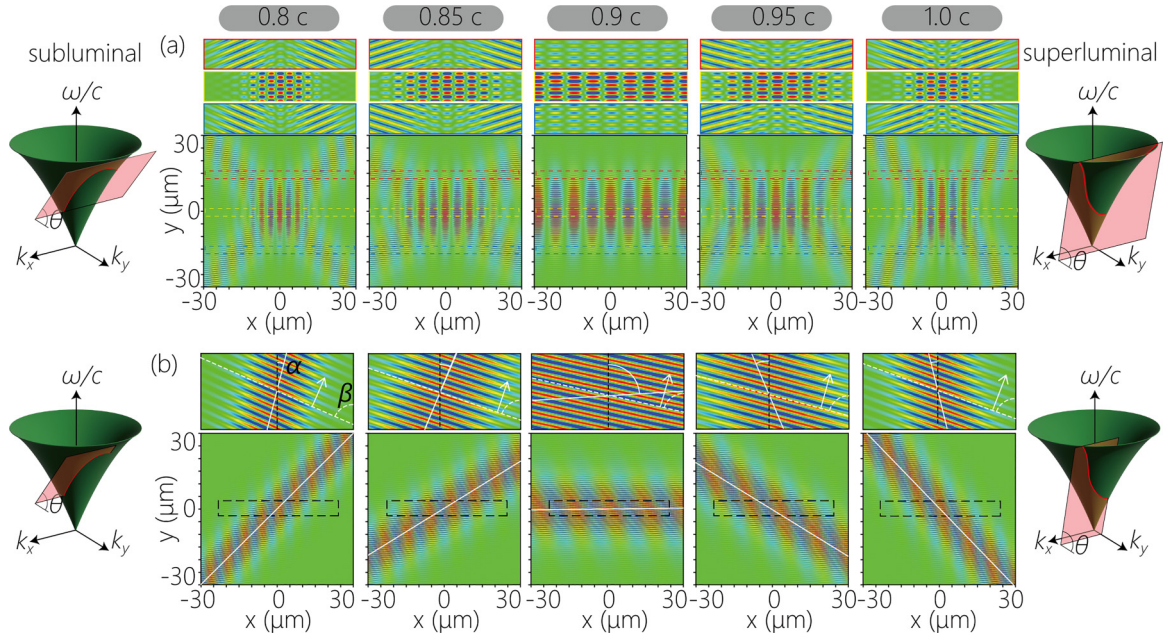


FIG. 5. (a) Spatial distribution of the ST-SPP wave packet, $\text{Re}[E_z(x, y; t = 0)]$ for different group velocities ranging from $0.8c$ to $1.0c$. Top panels show the expanded views indicated by dashed squares. The colors of the frames (red, yellow, and blue) correspond to the colors of the dashed squares in the main panels. (b) One of the two branch structures that make up the ST-SPP wave packet, calculated with only the positive k_x component. Top panels show the expanded views indicated by black dashed squares. White solid lines in the main panels and dashed lines in the top panels indicate the peak positions of the band structure itself and wave fronts of inside the band structures. White arrows are the normal direction of the wave front and correspond to the propagate directions. The angles between each line and the y axis were defined as α and β . Note that α and β are not comparable quantities since the aspect ratio of the expanded views has been modified.

where we have defined the parallel component of the electric field, $\mathbf{E}_{\parallel} = \mathbf{E} - E_z \mathbf{u}_z$, and the derivative in the direction parallel to the surface, $\nabla_{\parallel} := \mathbf{u}_x \partial_x + \mathbf{u}_y \partial_y$.

Once we get the electric field, the magnetic field can be calculated from Faraday's law of induction, $\nabla \times \mathbf{E} = \omega \mu_0 \mathbf{H}$, as follows:

$$\mathbf{H} = \frac{\nabla \times \mathbf{E}}{\omega \mu_0} = \frac{(\nabla_{\parallel} + k_z \mathbf{u}_z) \times (\mathbf{E}_{\parallel} + E_z \mathbf{u}_z)}{\omega \mu_0} \quad (\text{A4})$$

$$= i \frac{1 + k_z^2/k_{\text{sp}}^2}{\omega \mu_0} \mathbf{u}_z \times \nabla_{\parallel} E_z \quad (\text{A5})$$

$$= i \frac{\omega \epsilon \epsilon_0}{k_{\text{sp}}^2} \mathbf{u}_z \times \nabla_{\parallel} E_z. \quad (\text{A6})$$

Note that we have applied $k_{\text{sp}}^2 + k_z^2 = (\omega/c)^2 \epsilon$. Note also that the permittivity is dependent on whether we are on the dielectric or metal side,

$$\epsilon(z, \omega) = \begin{cases} \epsilon_d & (z > 0) \\ \epsilon_m(\omega) & (z < 0). \end{cases} \quad (\text{A7})$$

APPENDIX B: WAVEFRONT DIRECTIONS OF $\pm k_x$ BRANCHES

The electric spatial distribution, including fine fringes within the wave packet, is useful for visualizing the intricate motion of the ST-SPP wave packets. Figure 5 displays the real part of the electric field $E_z(x, y; t = 0)$ of the ST-SPP wave packets calculated for different group velocities ranging from $0.8c$ to $1.0c$. The expanded views of the dashed squares are plotted in the top panels.

All of the spatial distributions show that the subluminal and superluminal ST-SPP wave packets with close v_{diff} have similar envelope distributions, where v_{diff} is a difference of the group velocity between the ST-SPP wave packet and the conventional SPP wave packet ($v_{\text{diff}} = |v_{\text{sp}} - \tilde{v}_g|$). The angles $\pm \alpha$ of the $\pm k_x$ branches, which constitute the ST-SPP wave packet, depend on the angle θ of the spectral plane and vary with the group velocity. While the entire distribution of the wave packets corresponds, the fringes within the branches are oriented in contrasting directions in the superluminal and subluminal wave packets. The wave fronts of the subluminal ST-SPP are distributed in a rhombic shape surrounding the central region, whereas the wave fronts of the superluminal ST-SPP are distributed radially from the central region. In Fig. 5(b), we plotted the $+k_x$ branch calculated from only the $+k_x$ component of the ST-SPP wave packet. The angles between the wave front inside the branch made with the propagation axis are defined as β . The value of α varies widely with \tilde{v}_g , being negative during subluminal and positive during superluminal. In contrast, the group velocity dependence of β is relatively small compared to α , and the wave front faces the upper right direction regardless of v_g .

APPENDIX C: SPATIAL DISTRIBUTIONS OF THE FIELD INTENSITY, t -SAM_L, AND D OF ST-SPP

As discussed in Figs. 3 and 4 in the main text, the spatial distribution of the SAM and topological charge density are determined by the spatial distribution of the ST-SPP wave packet, which vary with the designed group velocity. In Figs. 6(a)–6(c), we plotted the $I(x, y; t = 0)$,

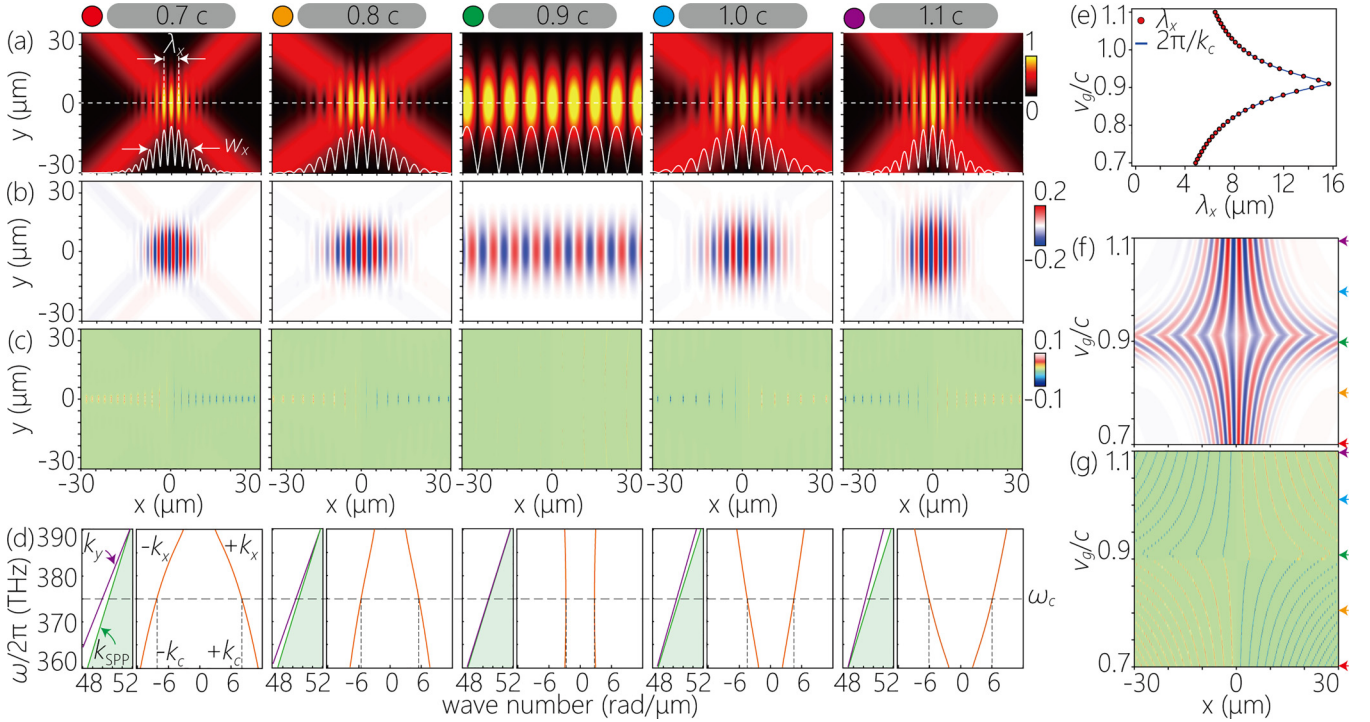


FIG. 6. (a)–(c) Spatial field distribution of the typical parameters of ST-SPP wave packets in physical space for various group velocities ranging from $0.7c$ to $1.1c$. (a) $I(x, y; t = 0)$, (b) $t\text{-SAM}_\perp(x, y; t = 0)$, and (c) $D(x, y; t = 0)$. White lines in (a) are cross sections along $y = 0$. (d) The spectral projections onto the (k_y, ω) and (k_x, ω) planes. (e) Transverse wave number of the ST-SPP wave packets. The red circles and blue line represent the λ_x evaluated from $I(x, y; t = 0)$ [shown in (a)] and $2\pi/k_c$ calculated from the spectral domain [shown in (d)], respectively. (f),(g) Variation of the (f) S_z and (g) D distribution with group velocity. The horizontal profiles correspond to the integral cross sections along the y direction of the $S_z(x, y; t = 0)$ and $D(x, y; t = 0)$ in the calculation region shown in (b) and (c), ($-30 < y < 30$) μm .

$t\text{-SAM}_\perp(x, y; t = 0)$, and $D(x, y; t = 0)$ calculated for different group velocities ranging from $0.7c$ to $1.1c$. The projections of the spectral support domains onto the (k_y, ω) and (k_x, ω) planes at each group velocity were plotted in Fig. 6(d).

In both the superluminal and subluminal cases, the spectral domain projected onto the (k_y, ω) plane moves away from the SPP dispersion curve as the v_{diff} increases. Therefore, the transverse wave number $k_x(\omega) = \sqrt{k_{\text{sp}}^2 - k_y^2}$ increases as v_{diff} increases, resulting in the transverse fringe density of the ST-SPP wave packet is at its lowest value at $\tilde{v}_g = v_{\text{sp}}$. Under the calculation conditions of this paper, in which the spectrum of the ST-SPP wave packet is assumed to have a Fourier-limited pulse with a peak at $\omega_c = 375$ THz, the transverse wavelength λ_x of the ST-SPP wave packet is expressed as $\lambda_x = 2\pi/k_c$ [Fig. 6(e)], where k_c is transverse wave number evaluated at ω_c [Fig. 6(d)].

Since a regional extension of the branches distributed on the $y = 0$ axis is determined by the angle of the branches, the transverse Gaussian spatial distribution of the envelope of the ST-SPP wave packet, w_x , also varies with v_g . This change of the spatial width can also be interpreted as a change in wave-packet width due to the difference in Δk_x . For $\tilde{v}_g \simeq v_{\text{sp}}$, the spectral domain in the (k_x, ω) plane shows a slight curvature but almost constant $|k_x|$, resulting in very small Δk_x . The spatial distribution of the wave packet is similar to that of a striped ST-SPP wave packet whose spectral domain is defined by the iso- k_x plane [70], and w_x is almost infinite. In contrast, for ST-SPP wave packets with large v_{diff} , the

difference between k_y and k_{sp} is larger for larger $\Omega = \omega_o - \omega$, resulting in large Δk_x . From Fig. 6, we can confirm the inverse correlation between Δk_x and w_x .

A two-dimensional plot of the cross sections of the $t\text{-SAM}_\perp$ [Fig. 6(b)] integrated along the y direction is plotted in Fig. 6(f). The vertical axis shows the group velocity normalized by the speed of light in a vacuum. Since the spatial distribution of the $t\text{-SAM}_\perp$ reflects the intensity profile of the ST-SPP wave packet, the $t\text{-SAM}_\perp$ becomes densely distributed in the central region as v_{diff} increases. In addition, the maximum intensity of the SAM also increases with increasing v_{diff} because finer fringes imply a larger gradient of the energy flow density. A two-dimensional plot of the integrated cross section of D plotted in Fig. 6(g) shows a spatial distribution corresponding to the SAM. The left-right reversal of the sign of D associated with the change in \tilde{v}_g discussed in the main text can be confirmed.

APPENDIX D: EFFECTS OF SPP ATTENUATION ON THE $t\text{-SAM}_\perp$ OF ST-SPP

Figures 7(a) and 7(b) show the distribution of $t\text{-SAM}_\perp$ when the ST-SPP wave packet propagates to $y = 100$ μm ($t = 334$ fs), with and without the effect of SPP attenuation included in the calculation, respectively. Figure 7(a) is a replot of the lower panel of Fig. 3(g), but with an enhanced color contrast for easy recognition of the $t\text{-SAM}_\perp$ near the X-shaped SPP branches. We can observe, in both Figs. 7(a)

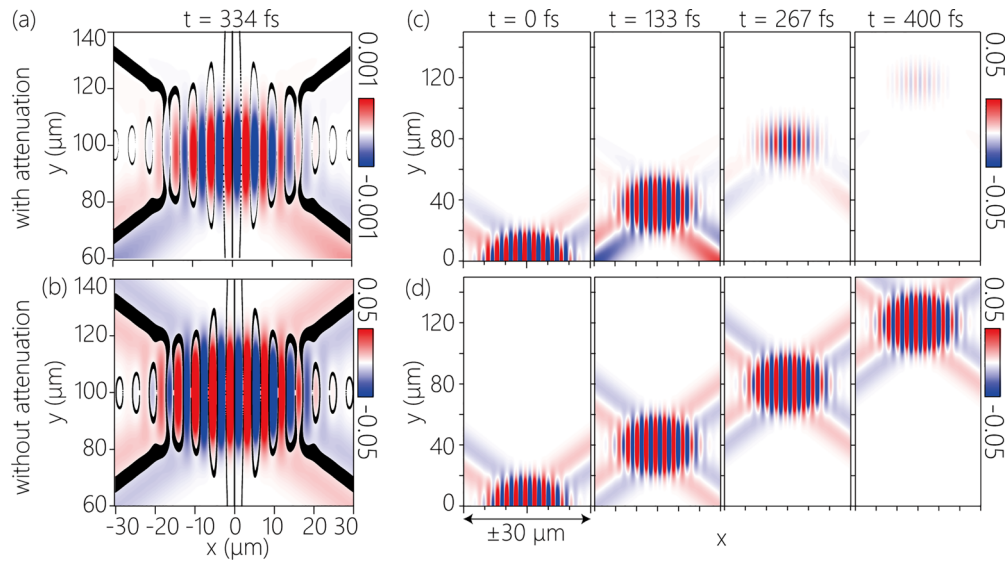


FIG. 7. (a),(b) Spatial distributions of the t -SAM $_{\perp}$ and L-lines of a ST-SPP wave packet propagated to $y = 100 \mu\text{m}$ ($t = 334 \text{ fs}$), (a) with and (b) without including the SPP attenuation. (c),(d) Series of t -SAM $_{\perp}$ distribution of a ST-SPP wave packet propagated to $y = 0, 40, 80,$ and $120 \mu\text{m}$, (c) with and (d) without including the SPP attenuation.

and 7(b), the faint t -SAM $_{\perp}$ intensities along the X-shaped branches (L-lines), in addition to the strong oscillatory distribution at the center part of the wave packet. The t -SAM $_{\perp}$ is caused by the spatial confinement of the SPP field. The magnitudes of t -SAM $_{\perp}$ are larger when the gradient of the field is steeper, resulting in the much weaker t -SAM $_{\perp}$ at the branches than at the center of the wave packet. Moreover, Fig. 7(a) shows that t -SAM $_{\perp}$ in the upper part of the branches is clearly weaker than that in the lower part. The field intensity is more strongly damped at the upper side due to the attenuation of the SPP wave, reflected in the weakening of t -SAM $_{\perp}$.

The effect of SPP attenuation on the t -SAM $_{\perp}$ distribution is more evident in the snapshots of the ST-SPP wave-packet propagation shown in Figs. 7(c) and 7(d). Figures 7(c) and 7(d) show the t -SAM $_{\perp}$ when the center of the ST-SPP wave packet propagates to $y = 0, 40, 80,$ and $120 \mu\text{m}$ with and without including the SPP attenuation, respectively. When SPP attenuation is ignored [Fig. 7(d)], both the wave-packet center and the X-shaped branch show a constant spatial

distribution and intensity of t -SAM $_{\perp}$, exhibiting a propagation invariance with suppression of both the diffraction- and the dispersion-induced deformations. In contrast, when SPP attenuation is taken into account [Fig. 7(c)], t -SAM $_{\perp}$ attenuates with the propagation in both the wave-packet center and the X-shaped branch. The attenuation length of SPP is connected to the imaginary part of the complex dispersion relation $k_{\text{SPP}}(\omega)$ as $\kappa = \frac{1}{2}\text{Im}[k_{\text{SPP}}]$, and is approximately $45 \mu\text{m}$ for an excitation light wavelength of 800 nm . This length is comparable to the size of the longitudinal spread of the center part of the ST-SPP wave packet. Therefore, the field attenuation at the upper side of the X-shaped branch is more pronounced than at the lower side, and so is the case for the t -SAM $_{\perp}$. Nevertheless, the stable and nondiffractive nature of the center part of the ST-SPP wave packet is maintained despite the overall attenuation of the SPP field, which well demonstrates the characteristics of the ST-SPP wave packet that can suppress the spatial spreading due to the dispersion relation.

-
- [1] J. H. Poynting, The wave motion of a revolving shaft, and a suggestion as to the angular momentum in a beam of circularly polarised light, *Proc. R. Soc. London A* **82**, 560 (1909).
- [2] R. A. Beth, Direct detection of the angular momentum of light, *Phys. Rev.* **48**, 471 (1935).
- [3] R. A. Beth, Mechanical detection and measurement of the angular momentum of light, *Phys. Rev.* **50**, 115 (1936).
- [4] T. Sugiura, S. Kawata, and S. Minami, Optical rotation of small particles by a circularly-polarized laser beam in an optical microscope, *J. Spectrosc. Soc. Jpn.* **39**, 342 (1990).
- [5] E. Higurashi, H. Ukita, H. Tanaka, and O. Ohguchi, Optically induced rotation of anisotropic micro-objects fabricated by surface micromachining, *Appl. Phys. Lett.* **64**, 2209 (1994).
- [6] E. Higurashi, O. Ohguchi, T. Tamamura, H. Ukita, and R. Sawada, Optically induced rotation of dissymmetrically shaped fluorinated polyimide micro-objects in optical traps, *J. Appl. Phys.* **82**, 2773 (1997).
- [7] M. Friese, T. Nieminen, N. Heckenberg, and H. Rubinsztein-Dunlop, Optical alignment and spinning of laser-trapped microscopic particles, *Nature (London)* **394**, 348 (1998).
- [8] J. Ahn, Z. Xu, J. Bang, Y.-H. Deng, T. M. Hoang, Q. Han, R.-M. Ma, and T. Li, Optically Levitated Nanodumbbell Torsion Balance and GHz Nanomechanical Rotor, *Phys. Rev. Lett.* **121**, 033603 (2018).
- [9] F. Monteiro, S. Ghosh, E. C. van Assendelft, and D. C. Moore, Optical rotation of levitated spheres in high vacuum, *Phys. Rev. A* **97**, 051802(R) (2018).
- [10] R. Reimann, M. Doderer, E. Hebestreit, R. Diehl, M. Frimmer, D. Windey, F. Tebbenjohanns, and L. Novotny, GHz Rotation

- of an Optically Trapped Nanoparticle in Vacuum, *Phys. Rev. Lett.* **121**, 033602 (2018).
- [11] Y. Jin, J. Yan, S. J. Rahman, J. Li, X. Yu, and J. Zhang, 6 GHz hyperfast rotation of an optically levitated nanoparticle in vacuum, *Photon. Res.* **9**, 1344 (2021).
- [12] A. Aiello, N. Lindlein, C. Marquardt, and G. Leuchs, Transverse Angular Momentum and Geometric Spin Hall Effect of Light, *Phys. Rev. Lett.* **103**, 100401 (2009).
- [13] A. Aiello, C. Marquardt, and G. Leuchs, Transverse angular momentum of photons, *Phys. Rev. A* **81**, 053838 (2010).
- [14] K. Y. Bliokh and F. Nori, Transverse and longitudinal angular momenta of light, *Phys. Rep.* **592**, 1 (2015).
- [15] A. Y. Bekshaev, Oblique section of a paraxial light beam: Criteria for azimuthal energy flow and orbital angular momentum, *J. Opt. A: Pure Appl. Opt.* **11**, 094003 (2009).
- [16] M. Antognozzi, C. Bermingham, R. Harniman, S. Simpson, J. Senior, R. Hayward, H. Hoerber, M. Dennis, A. Bekshaev, K. Bliokh *et al.*, Direct measurements of the extraordinary optical momentum and transverse spin-dependent force using a nanocantilever, *Nat. Phys.* **12**, 731 (2016).
- [17] A. Canaguier-Durand and C. Genet, Plasmonic lateral forces on chiral spheres, *J. Opt.* **18**, 015007 (2016).
- [18] A. Canaguier-Durand and C. Genet, Transverse spinning of a sphere in a plasmonic field, *Phys. Rev. A* **89**, 033841 (2014).
- [19] C. Junge, D. O'Shea, J. Volz, and A. Rauschenbeutel, Strong Coupling between Single Atoms and Nontransversal Photons, *Phys. Rev. Lett.* **110**, 213604 (2013).
- [20] A. Aiello, P. Banzer, M. Neugebauer, and G. Leuchs, From transverse angular momentum to photonic wheels, *Nat. Photon.* **9**, 789 (2015).
- [21] X. Zhang, B. Shen, Z. Zhu, G. Rui, J. He, Y. Cui, and B. Gu, Understanding of transverse spin angular momentum in tightly focused linearly polarized vortex beams, *Opt. Express* **30**, 5121 (2022).
- [22] D. R. Abujetas and J. A. Sanchez-Gil, Spin angular momentum of guided light induced by transverse confinement and intrinsic helicity, *ACS Photon.* **7**, 534 (2020).
- [23] A. Y. Bekshaev, K. Y. Bliokh, and F. Nori, Transverse Spin and Momentum in Two-Wave Interference, *Phys. Rev. X* **5**, 011039 (2015).
- [24] K. Y. Bliokh, A. Y. Bekshaev, and F. Nori, Extraordinary momentum and spin in evanescent waves, *Nat. Commun.* **5**, 3300 (2014).
- [25] Oleh Y. Yermakov, Anton I. Ovcharenko, Andrey A. Bogdanov, I. V. Iorsh, K. Y. Bliokh, and Y. S. Kivshar, Spin control of light with hyperbolic metasurfaces, *Phys. Rev. B* **94**, 075446 (2016).
- [26] K. Y. Bliokh, H. Punzmann, H. Xia, F. Nori, and M. Shats, Field theory spin and momentum in water waves, *Sci. Adv.* **8**, eabm1295 (2022).
- [27] K. Y. Bliokh and F. Nori, Transverse spin of a surface polariton, *Phys. Rev. A* **85**, 061801(R) (2012).
- [28] K.-Y. Kim, I.-M. Lee, J. Kim, J. Jung, and B. Lee, Time reversal and the spin angular momentum of transverse-electric and transverse-magnetic surface modes, *Phys. Rev. A* **86**, 063805 (2012).
- [29] K.-Y. Kim and A. X. Wang, Spin angular momentum of surface modes from the perspective of optical power flow, *Opt. Lett.* **40**, 2929 (2015).
- [30] K. Y. Bliokh, A. Y. Bekshaev, and F. Nori, Optical Momentum, Spin, and Angular Momentum in Dispersive Media, *Phys. Rev. Lett.* **119**, 073901 (2017).
- [31] Y. Dai, M. Dabrowski, V. A. Apkarian, and H. Petek, Ultrafast microscopy of spin-momentum-locked surface plasmon polaritons, *ACS Nano* **12**, 6588 (2018).
- [32] K. Y. Bliokh, D. Smirnova, and F. Nori, Quantum spin Hall effect of light, *Science* **348**, 1448 (2015).
- [33] T. V. Mechelen and Z. Jacob, Universal spin-momentum locking of evanescent waves, *Optica* **3**, 118 (2016).
- [34] D. O'Connor, P. Ginzburg, F. J. Rodriguez-Fortuno, G. A. Wurtz, and A. V. Zayats, Spin-orbit coupling in surface plasmon scattering by nanostructures, *Nat. Commun.* **5**, 5327 (2014).
- [35] F. J. Rodriguez-Fortuno, G. Marino, P. Ginzburg, D. O'Connor, A. Martinez, G. A. Wurtz, and A. V. Zayats, Near-field interference for the unidirectional excitation of electromagnetic guided modes, *Science* **340**, 328 (2013).
- [36] Y. Dai and H. Petek, Plasmonic spin-Hall effect in surface plasmon polariton focusing, *ACS Photon.* **6**, 2005 (2019).
- [37] P. Shi, L. Du, and X. Yuan, Spin photonics: From transverse spin to photonic skyrmions, *Nanophotonics* **10**, 3927 (2021).
- [38] F. Cardano and L. Marrucci, Spin-orbit photonics, *Nat. Photon.* **9**, 776 (2015).
- [39] L. Du, A. Yang, A. V. Zayats, and X. Yuan, Deep-subwavelength features of photonic skyrmions in a confined electromagnetic field with orbital angular momentum, *Nat. Phys.* **15**, 650 (2019).
- [40] Y. Dai, Z. Zhou, A. Ghosh, R. S. K. Mong, A. Kubo, C.-B. Huang, and H. Petek, Plasmonic topological quasiparticle on the nanometre and femtosecond scales, *Nature (London)* **588**, 616 (2020).
- [41] X. Lei, A. Yang, P. Shi, Z. Xie, L. Du, A. V. Zayats, and X. Yuan, Photonic Spin Lattices: Symmetry Constraints for Skyrmion and Meron Topologies, *Phys. Rev. Lett.* **127**, 237403 (2021).
- [42] Q. Zhang, Z. Xie, L. Du, P. Shi, and X. Yuan, Bloch-type photonic skyrmions in optical chiral multilayers, *Phys. Rev. Res.* **3**, 023109 (2021).
- [43] A. Ghosh, S. Yang, Y. Dai, Z. Zhou, T. Wang, C.-B. Huang, and H. Petek, A topological lattice of plasmonic merons, *Appl. Phys. Rev.* **8**, 041413 (2021).
- [44] Y. Dai, Z. Zhou, A. Ghosh, K. Kapoor, M. Dabrowski, A. Kubo, C.-B. Huang, and H. Petek, Ultrafast microscopy of a twisted plasmonic spin skyrmion, *Appl. Phys. Rev.* **9**, 011420 (2022).
- [45] P. Shi, L. Du, M. Li, and X. Yuan, Symmetry-protected photonic chiral spin textures by spin-orbit coupling, *Laser Photon. Rev.* **15**, 2000554 (2021).
- [46] P. Shi, L. Du, C. Li, A. V. Zayats, and X. Yuan, Transverse spin dynamics in structured electromagnetic guided waves, *Proc. Natl. Acad. Sci. USA* **118**, e2018816118 (2021).
- [47] C. Taneja, D. Paul, and G. V. P. Kumar, Experimental observation of transverse spin of plasmon polaritons in a single crystalline silver nanowire, *Appl. Phys. Lett.* **119**, 161108 (2021).
- [48] Y. Dai, A. Ghosh, S. Yang, Z. Zhou, C.-b. Huang, and H. Petek, Poincare engineering of surface plasmon polaritons, *Nat. Rev. Phys.* **4**, 562 (2022).

- [49] A. Ghosh, S. Yang, Y. Dai, and H. Petek, The spin texture topology of polygonal plasmon fields, *ACS Photon.* **10**, 13 (2023).
- [50] Y. Shen, E. C. Martinez, and C. Rosales-Guzman, Generation of optical skyrmions with tunable topological textures, *ACS Photon.* **9**, 296 (2022).
- [51] Y. Shen, Topological bimeronic beams, *Opt. Lett.* **46**, 3737 (2021).
- [52] Z.-L. Deng, T. Shi, A. Krasnok, X. Li, and A. Alu, Observation of localized magnetic plasmon skyrmions, *Nat. Commun.* **13**, 8 (2022).
- [53] L. Xiong, Y. Li, D. Halbertal, M. Sammon, Z. Sun, S. Liu, J. H. Edgar, T. Low, M. M. Fogler, C. R. Dean, A. J. Millis, and D. N. Basov, Polaritonic vortices with a half-integer charge, *Nano Lett.* **21**, 9256 (2021).
- [54] S. Tsesses, E. Ostrovsky, K. Cohen, B. Gjonaj, N. H. Lindner, and G. Bartal, Optical skyrmion lattice in evanescent electromagnetic fields, *Science* **361**, 993 (2018).
- [55] T. J. Davis, D. Janoschka, P. Dreher, B. Frank, F.-J. M. zu Heringdorf, and H. Giessen, Ultrafast vector imaging of plasmonic skyrmion dynamics with deep subwavelength resolution, *Science* **368**, eaba6415 (2020).
- [56] N. Nagaosa and Y. Tokura, Topological properties and dynamics of magnetic skyrmions, *Nat. Nanotechnol.* **8**, 899 (2013).
- [57] W. Jiang, P. Upadhyaya, W. Zhang, G. Yu, M. B. Jungfleisch, F. Y. Fradin, J. E. Pearson, Y. Tserkovnyak, K. L. Wang, O. Heinonen, S. G. E. te Velthuis, and A. Hoffmann, Blowing magnetic skyrmion bubbles, *Science* **349**, 283 (2015).
- [58] S. Woo, K. Litzius, B. Krueger, M.-Y. Im, L. Caretta, K. Richter, M. Mann, A. Krone, R. M. Reeve, M. Weigand, P. Agrawal, I. Lemesch, M.-A. Mawass, P. Fischer, M. Klauui, and G. R. S. D. Beach, Observation of room-temperature magnetic skyrmions and their current-driven dynamics in ultrathin metallic ferromagnets, *Nat. Mater.* **15**, 501 (2016).
- [59] W. Jiang, G. Chen, K. Liu, J. Zang, S. G. E. te Velthuis, and A. Hoffmann, Skyrmions in magnetic multilayers, *Phys. Rep.* **704**, 1 (2017).
- [60] S. L. Zhang, W. W. Wang, D. M. Burn, H. Peng, H. Berger, A. Bauer, C. Pfeleiderer, G. van der Laan, and T. Hesjedal, Manipulation of skyrmion motion by magnetic field gradients, *Nat. Commun.* **9**, 2115 (2018).
- [61] C. Bai, J. Chen, Y. Zhang, D. Zhang, and Q. Zhan, Dynamic tailoring of an optical skyrmion lattice in surface plasmon polaritons, *Opt. Express* **28**, 10320 (2020).
- [62] M. Lin, W. Zhang, C. Liu, L. Du, and X. Yuan, Photonic spin skyrmion with dynamic position control, *ACS Photon.* **8**, 2567 (2021).
- [63] N. Ichiji, Y. Otake, and A. Kubo, Femtosecond imaging of spatial deformation of surface plasmon polariton wave packet during resonant interaction with nanocavity, *Nanophotonics* **11**, 1321 (2022).
- [64] Y. Wang, C. Ming, Y. Zhang, J. Xu, F. Feng, L. Li, and X. Yuan, Spatiotemporal manipulation on focusing and propagation of surface plasmon polariton pulses, *Opt. Express* **28**, 33516 (2020).
- [65] A. Karalis and J. D. Joannopoulos, Plasmonic Metasurface “Bullets” and other “Moving Objects”: Spatiotemporal Dispersion Cancellation for Linear Passive Subwavelength Slow Light, *Phys. Rev. Lett.* **123**, 067403 (2019).
- [66] K. L. Schepler, M. Yessenov, Y. Zhiyenbayev, and A. F. Abouraddy, Space-time surface plasmon polaritons: A new propagation-invariant surface wave packet, *ACS Photon.* **7**, 2966 (2020).
- [67] H. E. Kondakci and A. F. Abouraddy, Diffraction-free space-time beams, *Nat. Photon.* **11**, 733 (2017).
- [68] B. Bhaduri, M. Yessenov, and A. F. Abouraddy, Meters-long propagation of diffraction-free space-time light sheets, *Opt. Express* **26**, 20111 (2018).
- [69] M. Yessenov, L. A. Hall, K. L. Schepler, and A. F. Abouraddy, Space-time wave packets, *Adv. Opt. Photon.* **14**, 455 (2022).
- [70] N. Ichiji, H. Kikuchi, M. Yessenov, K. L. Schepler, A. F. Abouraddy, and A. Kubo, Observation of ultrabroadband striped space-time surface plasmon polaritons, *ACS Photon.* **10**, 374 (2023).
- [71] N. Ichiji, M. Yessenov, K. L. Schepler, A. F. Abouraddy, and A. Kubo, Exciting space-time surface plasmon polaritons by irradiating a nanoslit structure, [arXiv:2212.05450](https://arxiv.org/abs/2212.05450).
- [72] N. Lassaline, R. Brechbuhler, S. J. W. Vonk, K. Ridderbeek, M. Spieser, S. Bisig, B. Le Feber, F. T. Rabouw, and D. J. Norris, Optical fourier surfaces, *Nature (London)* **582**, 506 (2020).
- [73] A. D. Rakić, A. B. Djurišić, J. M. Elazar, and M. L. Majewski, Optical properties of metallic films for vertical-cavity optoelectronic devices, *Appl. Opt.* **37**, 5271 (1998).
- [74] A. Kubo, N. Pontius, and H. Petek, Femtosecond microscopy of surface plasmon polariton wave packet evolution at the silver/vacuum interface, *Nano Lett.* **7**, 470 (2007).
- [75] L. Zhang, A. Kubo, L. Wang, H. Petek, and T. Seideman, Imaging of surface plasmon polariton fields excited at a nanometer-scale slit, *Phys. Rev. B* **84**, 245442 (2011).
- [76] J. Lin, J. Dellinger, P. Genevet, B. Cluzel, F. de Fornel, and F. Capasso, Cosine-Gauss Plasmon Beam: A Localized Long-Range Nondiffracting Surface Wave, *Phys. Rev. Lett.* **109**, 093904 (2012).
- [77] H. E. Kondakci and A. F. Abouraddy, Optical space-time wave packets of arbitrary group velocity in free space, *Nat. Commun.* **10**, 929 (2019).
- [78] M. Yessenov and A. F. Abouraddy, Accelerating and Decelerating Space-Time Optical Wave Packets in Free Space, *Phys. Rev. Lett.* **125**, 233901 (2020).
- [79] L. A. Hall, M. Yessenov, and A. F. Abouraddy, Arbitrarily accelerating space-time wave packets, *Opt. Lett.* **47**, 694 (2022).
- [80] M. Yessenov, L. A. Hall, and A. F. Abouraddy, Engineering the optical vacuum: Arbitrary magnitude, sign, and order of dispersion in free space using space-time wave packets, *ACS Photon.* **8**, 2274 (2021).
- [81] L. A. Hall and A. F. Abouraddy, Free-space group-velocity dispersion induced in space-time wave packets by v-shaped spectra, *Phys. Rev. A* **104**, 013505 (2021).
- [82] H. He, C. Guo, and M. Xiao, Nondispersive space-time wave packets propagating in dispersive media, *Laser Photon. Rev.* **16**, 2100634 (2022).
- [83] P. Saari and K. Reivelt, Evidence of X-Shaped Propagation-Invariant Localized Light Waves, *Phys. Rev. Lett.* **79**, 4135 (1997).
- [84] J. N. Brittingham, Focus waves modes in homogeneous Maxwell's equations: Transverse electric mode, *J. Appl. Phys.* **54**, 1179 (1983).

- [85] A. Sezginer, A general formulation of focus wave modes, *J. Appl. Phys.* **57**, 678 (1985).
- [86] J. Dumin, J. J. Miceli, and J. H. Eberly, Diffraction-Free Beams, *Phys. Rev. Lett.* **58**, 1499 (1987).
- [87] F. Gori, G. Guattari, and C. Padovani, Bessel-Gauss beams, *Opt. Commun.* **64**, 491 (1987).
- [88] M. Yessenov, B. Bhaduri, L. Mach, D. Mardani, H. E. Kondakci, M. A. Alonso, G. A. Atia, and A. F. Abouraddy, What is the maximum differential group delay achievable by a space-time wave packet in free space? *Opt. Express* **27**, 12443 (2019).
- [89] A. Y. Bekshaev and M. Soskin, Transverse energy flows in vectorial fields of paraxial beams with singularities, *Opt. Commun.* **271**, 332 (2007).
- [90] M. V. Berry, Optical currents, *J. Opt. A* **11**, 094001 (2009).
- [91] A. Bekshaev, K. Y. Bliokh, and M. Soskin, Internal flows and energy circulation in light beams, *J. Opt.* **13**, 053001 (2011).
- [92] A. Y. Bekshaev, Subwavelength particles in an inhomogeneous light field: Optical forces associated with the spin and orbital energy flows, *J. Opt.* **15**, 044004 (2013).
- [93] T. Fösel, V. Peano, and F. Marquardt, L lines, C points and Chern numbers: Understanding band structure topology using polarization fields, *New J. Phys.* **19**, 115013 (2017).
- [94] M. Dennis, Polarization singularities in paraxial vector fields: Morphology and statistics, *Opt. Commun.* **213**, 201 (2002).
- [95] M. Neugebauer, T. Bauer, A. Aiello, and P. Banzer, Measuring the Transverse Spin Density of Light, *Phys. Rev. Lett.* **114**, 063901 (2015).
- [96] J. Deschamps, M. Fitaire, and M. Lagoutte, Inverse Faraday Effect in a Plasma, *Phys. Rev. Lett.* **25**, 1330 (1970).
- [97] Z. M. Sheng and J. Meyer-ter-Vehn, Inverse Faraday effect and propagation of circularly polarized intense laser beams in plasmas, *Phys. Rev. E* **54**, 1833 (1996).
- [98] R. Hertel, Theory of the inverse Faraday effect in metals, *J. Magn. Magn. Mater.* **303**, L1 (2006).
- [99] H.-L. Zhang, Y.-Z. Wang, and X.-J. Chen, A simple explanation for the inverse Faraday effect in metals, *J. Magn. Magn. Mater.* **321**, L73 (2009).
- [100] D. Oue and M. Matsuo, Electron spin transport driven by surface plasmon polaritons, *Phys. Rev. B* **101**, 161404(R) (2020).
- [101] T. J. Wijaya, D. Oue, M. Matsuo, Y. Ito, K. Elphick, H. Uchida, M. Inoue, and A. Hirohata, Spin current generation by a surface plasmon polariton. [arXiv:2004.12348](https://arxiv.org/abs/2004.12348).
- [102] A. Bekshaev, Spin-accumulation and spin-transport effects induced by surface plasmon-polariton waves, *J. Opt. Soc. Am. B* **39**, 3187 (2022).
- [103] D. Oue and M. Matsuo, Effects of surface plasmons on spin currents in a thin film system, *New J. Phys.* **22**, 033040 (2020).
- [104] D. Oue and M. Matsuo, Optically induced electron spin currents in the Kretschmann configuration, *Phys. Rev. B* **102**, 125431 (2020).
- [105] M. S. Ukhtary, Y. Tian, and R. Saito, Spin current generation by edge plasmons in graphene ribbons, *Phys. Rev. B* **103**, 245428 (2021).
- [106] Y. Tian, M. S. Ukhtary, and R. Saito, Switching performance of optically generated spin current at the graphene edge, *Phys. Rev. B* **106**, 045420 (2022).
- [107] B. Göbel, I. Mertig, and O. A. Tretiakov, Beyond skyrmions: Review and perspectives of alternative magnetic quasiparticles, *Phys. Rep.* **895**, 1 (2021).
- [108] S.-H. Yang, R. Naaman, Y. Paltiel, and S. S. P. Parkin, Chiral spintronics, *Nat. Rev. Phys.* **3**, 328 (2021).
- [109] K. Hamamoto, M. Ezawa, and N. Nagaosa, Purely electrical detection of a skyrmion in constricted geometry, *Appl. Phys. Lett.* **108**, 112401 (2016).
- [110] D. Maccariello, W. Legrand, N. Reyren, K. Garcia, K. Bouzouhane, S. Collin, V. Cros, and A. Fert, Electrical detection of single magnetic skyrmions in metallic multilayers at room temperature, *Nat. Nanotechnol.* **13**, 233 (2018).
- [111] T. Schulz, R. Ritz, A. Bauer, M. Halder, M. Wagner, C. Franz, C. Pfleiderer, K. Everschor, M. Garst, and A. Rosch, Emergent electrodynamic of skyrmions in a chiral magnet, *Nat. Phys.* **8**, 301 (2012).
- [112] P. Bruno, V. K. Dugaev, and M. Taillefumier, Topological Hall Effect and Berry Phase in Magnetic Nanostructures, *Phys. Rev. Lett.* **93**, 096806 (2004).
- [113] A. Neubauer, C. Pfleiderer, B. Binz, A. Rosch, R. Ritz, P. G. Niklowitz, and P. Böni, Topological Hall Effect in the A Phase of MnSi, *Phys. Rev. Lett.* **102**, 186602 (2009).
- [114] M. Lee, W. Kang, Y. Onose, Y. Tokura, and N. P. Ong, Unusual Hall Effect Anomaly in MnSi Under Pressure, *Phys. Rev. Lett.* **102**, 186601 (2009).
- [115] Y. Jiang, H. Y. Yuan, Z.-X. Li, Z. Wang, H. W. Zhang, Y. Cao, and P. Yan, Twisted Magnon as a Magnetic Tweezer, *Phys. Rev. Lett.* **124**, 217204 (2020).
- [116] A. Karnieli, S. Tseses, G. Bartal, and A. Arie, Emulating spin transport with nonlinear optics, from high-order skyrmions to the topological Hall effect, *Nat. Commun.* **12**, 1092 (2021).
- [117] A. Nisbet, Hertzian electromagnetic potentials and associated gauge transformations, *Proc. R. Soc. London A* **231**, 250 (1955).
- [118] S. Hacyan, R. Jáuregui, F. Soto, and C. Villarreal, Spectrum of electromagnetic fluctuations in the Casimir effect, *J. Phys. A: Math. Gen.* **23**, 2401 (1990).
- [119] J. D. Jackson, *Classical Electrodynamics*, 3rd ed. (Wiley, New York, 1999).